Spectroscopy and electronic structure of Sr_2YRuO_6 and $Sr_2YRu_{0.75}Ir_{0.25}O_6$

E. B. Guedes,[1,*] M. Abbate,[1] F. Abud,[2] R. F. Jardim,[2] F. C. Vicentin,[3] and R. J. O. Mossanek[1]

[1]*Departamento de Física, Universidade Federal do Paraná, Caixa Postal 19044, 81531-990 Curitiba-PR, Brazil*
[2]*Instituto de Física, Universidade de São Paulo, 05315-970 São Paulo-SP, Brazil*
[3]*Laboratório Nacional de Luz Síncrotron, Caixa Postal 6192, 13083-970 Campinas-SP, Brazil*

We study the electronic structure of the Sr_2YRuO_6 and $Sr_2YRu_{0.75}Ir_{0.25}O_6$ compounds using x-ray (resonant) photoemission and absorption spectroscopies. The experimental results are interpreted with first-principles calculations, which give a good agreement with all the spectra. These results show that, although the spin-orbit coupling does not induce orbital anisotropies in these systems, it is responsible for the reduction of magnetic moments within the the $Ir^{5+}O_6$ octahedra, weakening the magnetic ordering in the substituted system. Finally, our findings support the idea that the canting of Ru^{5+} magnetic moments actually plays an important role in the stabilization of the intriguing magnetic ordering in the Sr_2YRuO_6 compound.

I. INTRODUCTION

Ruthenium-based perovskites form an intriguing class of materials, which exhibits physical properties ranging from itinerant ferromagnetism in distorted perovskite $SrRuO_3$ (SRO) [1] to superconductivity in the layered perovskite Sr_2RuO_4 [2]. Replacing every other Ru ion for Y in SRO leads to the antiferromagnetic semiconductor Sr_2YRuO_6 (SYRO). Although this material has been studied for almost four decades [3–5], the origin of some of its physical properties is not completely understood.

SYRO crystallizes in the monoclinic double-perovskite structure with space group $P2_1/n$, in which the RuO_6 and YO_6 octahedra form a three-dimensional (3D) checkerboardlike arrangement. In this structure, the deviation from the ideal cubic perovskite and the volume of the RuO_6 octahedra are larger than in the parent compound $SrRuO_3$. In the ionic limit, the divalent Sr^{2+} and trivalent Y^{3+} ions would present an empty $4d$ band, whereas the pentavalent Ru^{5+} ions would show a high-spin $4d^3$ ($^4A_{2g}$ symmetry) electronic configuration, which is assumed to possess quenched orbital angular momentum [6].

Electrical resistivity measurements of SYRO single crystals showed an uncommon semiconductor behavior [6]. Particularly in the $10\,\text{K} < T < 40\,\text{K}$ range, different scattering processes take place and negative magnetoresistance is observed. In the crystallographic ab plane, the electrical resistivity is consistent with an activation gap of 76 meV, while this gap for c is 120 meV [6], which could indicate an anisotropic electronic structure.

Although magnetic interactions are thought to arise only from Ru^{5+} ions, SYRO presents two phase transitions, one at $T_{N2} \sim 24\,\text{K}$ and the other at $T_{N1} \sim 32\,\text{K}$ [4,5]. The former marks the onset of the type-I antiferromagnetic (AFM) ordering, and the latter a transition to a fully AFM state [7]. The Ru^{5+} ions form a face-centered-cubic (fcc) network, which is believed to have key role in the anomalous properties of SYRO. This arrangement is the simplest 3D structure leading to frustrated magnetism [8], although long-range order was shown to be stabilized by next-nearest-neighbor (NNN) interactions and/or weak anisotropy [8–10].

Magnetic measurements in single crystals revealed the occurrence of weak ferromagnetism [6], which was attributed to canting of magnetic moments due to Dzyaloshinsky-Moriya interactions [11,12]. However, Singh and Tomy argued that the reported anomalous magnetic behavior of this compound cannot be explained by these interactions only [11], while structural changes have also been claimed to be responsible for determining the magnetic ground state of SYRO [12]. More recently, Granado and co-workers revealed the existence of two-dimensional magnetic correlations in this system and proposed a partially ordered state between T_{N2} and T_{N1}, stabilized by ferromagnetic interactions between nonconsecutive $YRuO_4$ layers in the 3D fcc lattice [7,13].

With respect to the electronic structure of Sr_2YRuO_6, the only theoretical work reported was done by Singh and Mazin [14], where results from local spin density approximation (LSDA) and tight-binding calculations are analyzed. Their calculations correctly captured the antiferromagnetic semiconducting ground state, as well as predicted the competition between ferromagnetic and antiferromagnetic interactions in this system. The calculated magnetic moments on the Ru (O) sites yielded $1.70\,\mu_B/\text{Ru}$ ion ($0.10\,\mu_B/\text{O}$ ion) and a small gap of 0.08 eV was found, in good agreement with neutron diffraction data [7]. Analysis of the calculated density of states resulted in an average occupancy of five electrons in the Ru $4d$ orbitals, similar to the parent compound $SrRuO_3$, indicating strong Ru–O covalence. Concerning experimental data, the only study found so far presents x-ray absorption measurements at Ru K, Ru L_3, and O K edges of the $Sr_2YRu_{1-x}Cu_xO_6$ system, motivated by the reports of superconductivity in this series [15,16].

One possible approach to study the magnetic interactions in SYRO is to replace Ru for other magnetic transition metals (TM). A good candidate is Ir because its 5+ ion possesses almost the same Shannon radii as Ru^{5+} [17], which would cause negligible change in the crystal structure of the compound. This substitution not only introduces a less magnetic atom in the Ru^{5+} fcc network, but it also

---

*guedes@fisica.ufpr.br

donates one extra electron to the system. There has not been any experimental nor theoretical work reported on the electronic structure of the $Sr_2YRu_{1-x}Ir_xO_6$ system so far.

Here, we study the electronic structure of the $x = 0$ and 0.25 members of the $Sr_2YRu_{1-x}Ir_xO_6$ series. The techniques employed are the (resonant) x-ray photoemission and absorption spectroscopies, which, to our knowledge, were never reported in these materials. In turn, these are interpreted with first-principles DFT calculations. The experimental spectra reveal the total and partial character of the valence and conduction bands, whereas the calculation, which is in good agreement with the experiment, gives information on magnetization, orbital occupancy, and spin-orbit effects on these systems. These are then used to explain the changes in the physical properties induced by the Ir substitution, which, finally, can help understanding some aspects of the complex magnetic ground state of SYRO.

II. EXPERIMENTAL DETAILS

Polycrystalline samples of $Sr_2YRu_{1-x}Ir_xO_6$, $x = 0$ and 0.25, were synthesized by the solid-state reaction method, as described in detail elsewhere [7]. Appropriated amounts of RuO_2, IrO_2, $SrCO_3$, and Y_2O_3 were ground together in an agate mortar, accommodated in an alumina crucible, and heat treated at $900\,°C$ in air for two days. The product was reground, pelletized, and subjected to another heat treatment carried out at $1250\,°C$ in air for approximately four days with intermediate grinding steps. Phase identification and unit-cell parameters were determined by refining powder x-ray diffraction patterns from a Bruker D8 Discovery diffractometer (Cu K_α radiation, $\lambda = 1.541$ Å) using the Rietveld method (GSAS/EXPGUI package) [18,19]. The measurements were performed at room temperature in the $15° < 2\theta < 120°$ range with a $0.05°$ step size and 2.0 s counting time. Magnetization $M(T)$ measurements were performed in a commercial SQUID magnetometer from Quantum Design in the temperature range between 5 and 300 K under zero-field-cooled (ZFC) and field-cooled (FC) conditions.

The spectroscopic measurements were carried out at the Laboratório Nacional de Luz Síncrotron in Campinas, Brazil. All the spectra were taken at room temperature with a base pressure of about 1.0×10^{-9} mbar. The (resonant) photoemission spectra were measured at the SXS beamline [20]. Photon energies were set to 2830 eV for the conventional photoemission (PES) and $\sim$2481 eV for the Ru $4p \rightarrow 4d$ resonant photoemisson (RPES). At these photon energies, the photoelectron escape depth is around 30 Å [21]. The overall energy resolution was about 0.5 eV for both PES and RPES measurements and the Fermi energy was calibrated using a clean Au foil. The O $1s$ edge x-ray absorption spectra were measured at the PGM beamline in the total electron yield mode. The energy resolution was about 0.4 eV, and the energy scale was calibrated using reference samples.

III. CALCULATION DETAILS

The band-structure calculations were carried out within the full potential linearized augmented plane wave + localized orbitals method, as implemented in the WIEN2K package [22,23], using the PBE-sol exchange-correlation potential [24]. The **k** integration was carried out using 172 points in the irreducible part of the first Brillouin zone, and the energy convergence was set to 1×10^{-5} eV.

Paramagnetic (P), ferromagnetic (FM), and AFM orderings were admitted. The P and FM solutions for both compounds were found using the experimental monoclinic crystal structure determined by neutron diffraction measurements. In turn, the AFM solution was obtained using a supercell of $2 \times 2 \times 1$ derived from the experimental monoclinic structure. This supercell can be seen as a pseudocubic structure, with lattice parameters $a' \sim b' \sim c'$, as described in Ref. [7]. This arrangement results in a Ru^{5+} fcc network with four equivalent ruthenium atoms, split into two subnetworks polarized antiparallel to each other. Then, the 25% substitution of Ru for Ir was simulated by replacing one Ru atom by an Ir atom of both equal and opposite spin polarizations. Self-consistent iterations lead both calculations to the same ground state, which preserves the spin polarization of the substituted Ru atom. As mentioned, this substitution causes a very small change in the lattice parameters, as confirmed by the following results. For this reason, the same crystal structure was used for the Sr_2YRuO_6 and $Sr_2YRu_{0.75}Ir_{0.25}O_6$ calculations.

It has been shown recently that spin-orbit (SO) coupling can lead to novel physics, particularly in 5d TMs [25–27]. In light of this fact, SO coupling was included in all transition metal (TM) valence d orbitals via the second variational method, as implemented in the WIEN2K package [22,23]. It is then necessary to establish a magnetization axis **M**. Since recent neutron diffraction measurements have shown that the spins align in the monoclinic b direction, the direction of **M** can be uniquely defined by the angle α, depicted in Fig. 1(b).
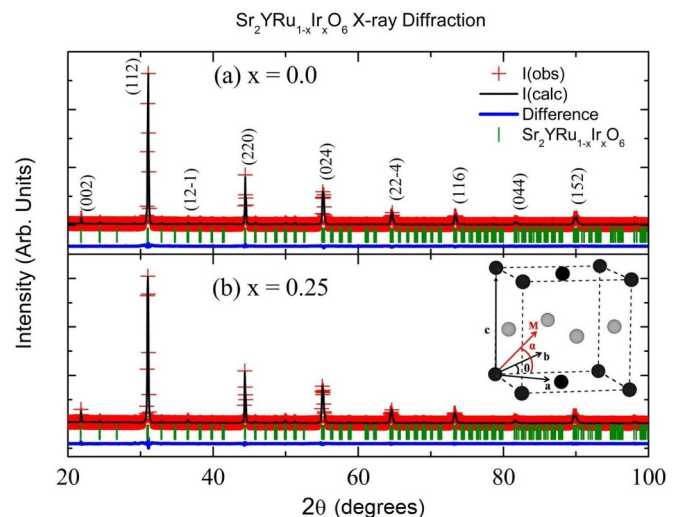

FIG. 1. X-ray diffraction patterns of the SRY(I)O samples with $x = 0$ (a) and 0.25 (b). The observed (red sign), calculated (black solid line), and difference (blue solid line) diagrams are displayed in the figure. The Rietveld profiles were obtained from diagrams taken at room temperature. The green bars represent the Bragg reflections of the Sr_2RuYO_6 crystal phase. Miller indices of some prominent peaks are marked in (a).

IV. RESULTS

A. Sample characterization

The expanded x-ray diffraction (XRD) patterns of the two studied samples $Sr_2Ru_{1-x}Ir_xYO_6$, $x = 0$ and 0.25, are displayed in Fig. 1. The observed reflections of the unsubstituted compound are very sharp and were indexed on the basis of a monoclinic unit cell, space group $P2_1/n$ [5,7,12], with lattice parameters $a = 5.7694$ Å, $b = 5.7782$ Å, and $c = 8.1617$ Å, in excellent agreement with the ones described elsewhere [28]. The partial Ru substitution by Ir has little effect in the XRD diagram [see Fig. 1(b)], except for two main features: (i) the monoclinic unit cell, space group $P2_1/n$, is preserved; and (ii) the Bragg peaks are slightly broadened, as commonly seen in solid solutions, and shifted a little to lower 2θ angles. The latter is consistent with the substitution of a slightly larger ion (Ir^{5+}) at the B site of the perovskite structure [17], a feature observed in the small but perceptible shift of the angular position of the Bragg reflections. Accordingly, the refined lattice parameters of the $x = 0.25$ sample, $a = 5.7657$ Å, $b = 5.7829$ Å, and $c = 8.1649$ Å, were found to be changing toward those of the Sr_2IrYO_6 crystal phase [29,30].

The temperature dependence of the magnetic susceptibility $\chi(T) = M(T)/H$, in the temperature range 5–90 K under an applied magnetic field of $H = 1$ kOe, for samples $Sr_2YRu_{1-x}Ir_xO_6$, $x = 0$ and 0.25, is displayed in Fig. 2. The $\chi(T)$ curves, conducted in zero-field-cooled (ZFC) and field-cooled (FC) conditions, display different features for both specimens. The pristine compound exhibits two transition temperatures: (i) at an upper temperature $T_{N1} \sim 32$ K in the ZFC curve, probably related to the coupling of alternative $YRuO_4$ layers antiferromagnetically, as inferred from neutron diffraction data [7]; and (ii) a similar transition at a lower temperature $T_{N2} \sim 25$ K in the FC curve, which may be due to the ordering of a fully ordered AFM state [7]. The latter evolves

to a state in which $\chi(T)$ is essentially temperature independent and assumes high values when compared with the ZFC branch for $T < T_{N2}$. These features, along with the observed decrease of the magnitude of the peak in $\chi(T)$ with increasing applied magnetic field (not shown), suggest frustration in the system and the occurrence of weak ferromagnetism, as discussed for single crystals of Sr_2YRuO_6 [6].

The partial substitution of Ru by Ir has a remarkable effect in the $\chi(T)$ data: the magnetic susceptibility is reduced and the ZFC curve shows a broad peak with a maximum at $T_{N1} \sim 16$ K, probably due to the development of AFM order or by merging of the two transitions observed in the parent compound. Such a maximum is absent in the FC curve and the magnitude of $\chi(T)$ approaches an almost temperature-independent value, close to the one seen in the pristine compound, further indicating a complex magnetic ground state. We also mention that the magnetic ground state of the parent compound Sr_2YRuO_6 seems to be more complicated than it appears, considering the recent observation of both two-dimensional and three-dimensional dynamics resulting from frustration [31].

We have also found that both samples display paramagnetic behavior at temperatures $T \gg T_{N1}$, a feature confirmed by the linear behavior of the temperature-dependent inverse magnetic susceptibility $\chi^{-1}(T)$ shown in the inset of Fig. 2. Curie-Weiss fits to the $\chi^{-1}(T)$ versus T data over the paramagnetic region comprehended between 50 and 350 K yielded an effective moment $\mu_{\text{eff}} = 3.88\ \mu_B/$Ru for the Sr_2YRuO_6 compound, a value very close to $3.87\ \mu_B/$Ru of isolated Hund's rule ground state of Ru^{5+} ion, and in agreement with a previous study [4]. We have also found a smaller effective magnetic moment $\mu_{\text{eff}} = 2.86\ \mu_B/$Ru in the Ir-substituted sample. This value is in line with the $\mu_{\text{eff}} = 0.91\ \mu_B/$Ir extracted from the Curie-Weiss fit in the pure Sr_2YIrO_6 (SYIO) compound [30]. The negative Curie-Weiss temperatures Θ_{CW}, obtained from fits of $\chi^{-1}(T)$ curves under $H = 5$ kOe, were $|\Theta_{\text{CW}}| \sim 292$ and 214 K, for samples with $x = 0$ and 0.25, respectively. The high values of $|\Theta_{\text{CW}}|$ resulted in frustration parameters $|\Theta_{\text{CW}}|/T_{N1} \sim 9$ (or ~ 12 when T_{N2} is considered) and ~ 13, respectively, further indicating the presence of magnetic frustration that increases little with increasing Ir content in this series.

B. Valence band photoemission spectra

The top panel of Fig. 3 shows the measured valence band (VB) photoemission spectra for the SYRO and SYRIO compounds. The spectra were obtained with a photon energy of 2830 eV and the solid line at zero energy denotes the Fermi energy. Both samples present insulating behavior and can be split into two major regions: (i) an O $2p$ derived band, split into bonding and nonbonding states, from around 10 eV to about 3 eV, and (ii) a Ru $4d$ (and Ir $5d$) rich region, from 3 to 0 eV. The main differences between both spectra are a slight shift in the O $2p$ band and a small increase in the relative intensity at the top and bottom of the valence band.

The bottom panel of Fig. 3 presents the calculated occupied densities of states (DOS) for both compositions, with the respective O $2p$, Ru $4d$, and Ir $5d$ projections. Since there are no reliable data on the photoionization cross section of each contribution for the photon energy used in the measurements,
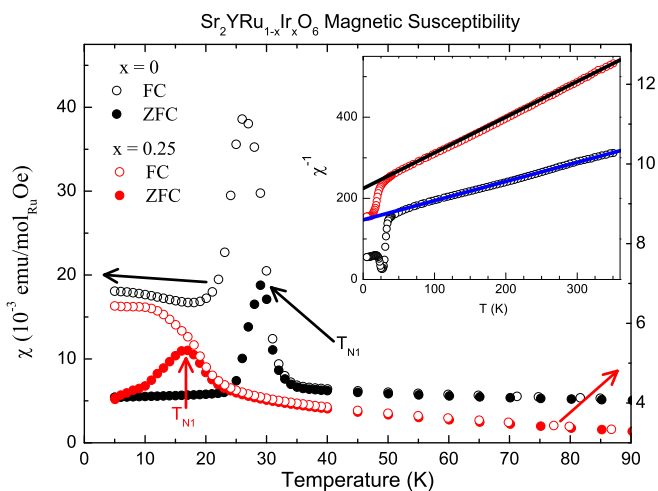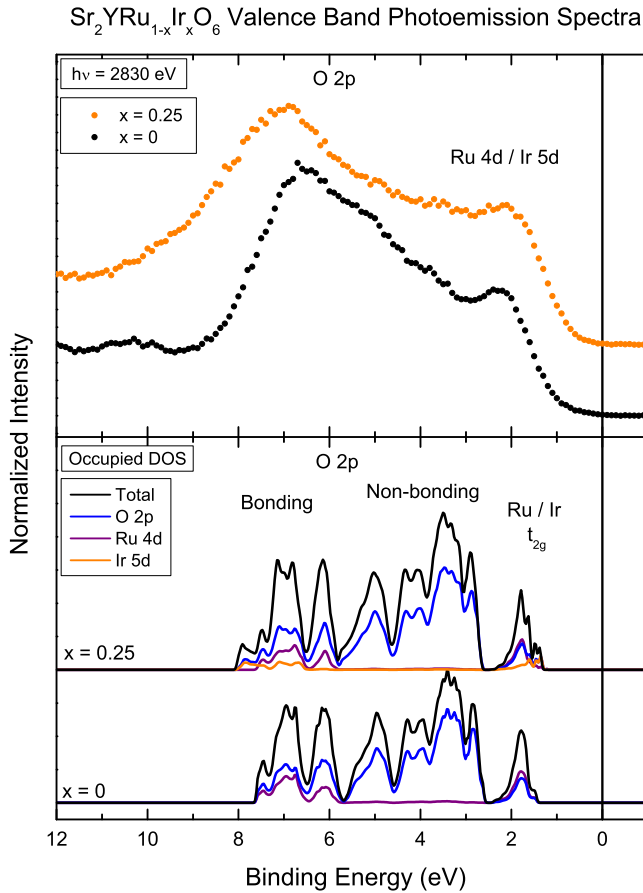

FIG. 2. Temperature dependence of the magnetic susceptibility $\chi(T) = M/H$, under an applied magnetic field of 1 kOe, for the two samples studied: Sr_2RuYO_6 and $Sr_2Ru_{0.75}Ir_{0.25}YO_6$. The inset displays the temperature dependence of the inverse magnetic susceptibility χ^{-1} and solid lines are linear fits of the data according to the Curie-Weiss law.

FIG. 3. Top: valence band photoemission spectra of Sr_2YRuO_6 and $Sr_2YRu_{0.75}Ir_{0.25}O_6$. Bottom: calculated occupied densities of states (DOS) for both compositions. The total DOS is projected into the O $2p$, Ru $4d$, and Ir $5d$ contributions.

FIG. 4. Ru L_3 resonant photoemission spectra (RPES) of Sr_2YRuO_6 and $Sr_2YRu_{0.75}Ir_{0.25}O_6$. The inset shows the Ru L_3 x-ray absorption spectra (XAS) of the samples, where the arrows indicate the photon energies used in RPES. The ON1 (2840.8 eV) and the ON2 (2843.6 eV) spectra are subtracted from the OFF (2830 eV) spectrum and compared to the calculated Ru $4d$ DOS.

the calculations were not corrected for this effect. However, the values at $h\nu = 1500$ eV give $\sigma_{Ru4d}/\sigma_{O2p}$ and $\sigma_{Ir5d}/\sigma_{O2p}$ ratios of around 36 and 62, respectively [21]. Allowing these ratios to be at least of the same order for $h\nu = 2830$ eV, this correction would then increase the relative intensity of the Ru $4d$ and Ir $5d$ states, thus being in good agreement with the valence band photoemission spectra.

According to the simulation, the Ru $4d$ states appear at the top and bottom of the valence band, mixed with O $2p$ states, and are mainly responsible for the two prominent structures in the experimental spectra. Further, the Ir $5d$ states appear closer to the Fermi energy than the Ru $4d$ states, in the $x = 0.25$ calculation, and also at the bottom of the valence band, which is consistent with the small increase in spectral weight at these energy regions. Finally, the spectra from 3 to 6 eV are dominated by almost pure nonbonding O $2p$ states.

C. Resonant photoemission spectra

Figure 4 presents the Ru L_3 resonant photoemission spectra (RPES) of Sr_2YRuO_6 and $Sr_2YRu_{0.75}Ir_{0.25}O_6$. The top and bottom panels show the OFF, ON1, and ON2 spectra for the SYRO and SYRIO compounds, respectively. The lines indicate the subtraction of the ON relative to the OFF spectrum,
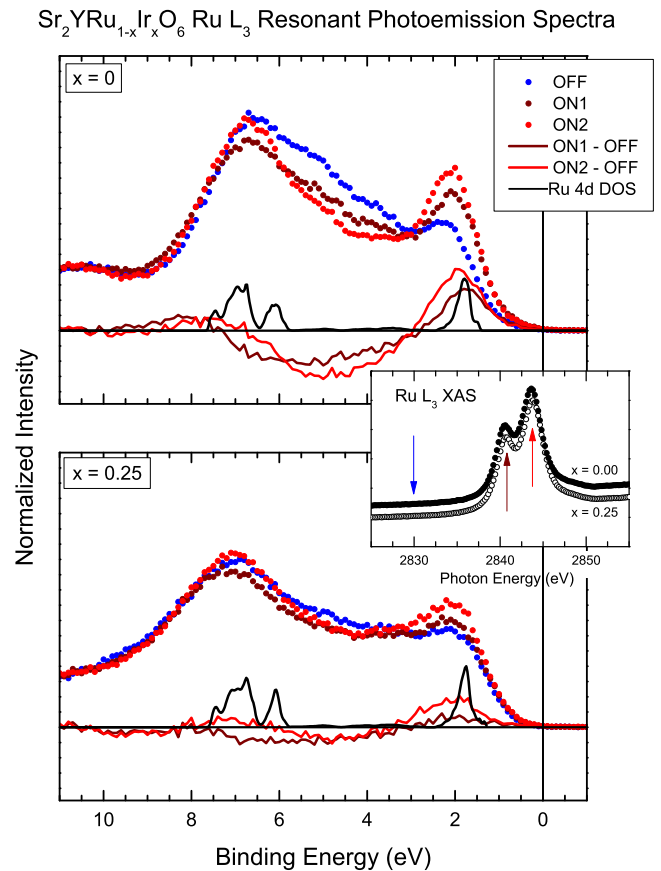
which are compared to the Ru $4d$ projection of the calculated occupied DOS.

The inset shows the Ru L_3 x-ray absorption spectra (XAS) of the samples, where the arrows indicate the photon energies used in the RPES. The off-resonance spectrum (OFF) was obtained at 2830 eV, whereas the two on-resonance spectra were taken at 2840.8 eV (ON1) and 2843.6 eV (ON2). The energy separation of the corresponding structures in the XAS spectra, which is about 3.8 eV, is consistent to the crystal-field splitting 10 Dq in these compounds (see below). Thus, the first energy is mainly related to transitions from the Ru $2p_{3/2}$ level to the unoccupied Ru $4d$ t_{2g} states, whereas the second is mostly related to transitions from the Ru $2p_{3/2}$ level to the unoccupied Ru $4d$ e_g states.

At the off-resonance condition, the spectrum is due to the direct photoemission process [32], namely, $2p^6 4d^n + h\nu \rightarrow 2p^6 4d^{n-1} + e^-$. However, at the on-resonance condition, the spectrum is enhanced due to interference with the indirect excitation channel $2p^6 4d^n + h\nu \rightarrow 2p^5 4d^{n+1} \rightarrow 2p^6 4d^{n-1} + e^-$. Thus, the ON-OFF spectrum is directly related to the Ru $4d$ character in the valence band due to the virtual $2p^5 4d^{n+1}$ excitation. The present Ru L high-energy RPES presents some advantages in comparison to N RPES and the Cooper

minimum methods. Effects of photoionization cross section are not present here because the energy difference is small (about 0.4%); the spectra are less surface sensitive because the photoelectron escape depth is around 30 Å [21]; and the signal enhancement due to the L edge absorption is large enough to provide satisfactory signal-to-noise ratio.

The positive enhancement to the spectra in the ON(1,2) conditions appears close to the Fermi energy, around 0 and 3 eV, and at the bottom of the valence band, about 6 to 9 eV, which is in line with the calculated DOS. The main differences between each system are the relative intensity of the RPES signal, which is higher for the SYRO system. Further, the RPES enhancement at the bottom of the valence band appears at lower binding energies, in the SYRIO compound.

The RPES spectra of both systems are somewhat different than for SrRuO₃ [33], where the Ru^{4+} ions show a low-spin $4d^4$ electronic configuration. In the latter, a positive RPES signal appears close to the Fermi energy, but also at around 4 eV, showing a considerable amount of Ru $4d$ weight in the O $2p$ region. Further, the SRO RPES spectrum presents significant intensity at approximately 10 eV. The differences found in the Ru $4d$ spectral weight cannot be understood in terms of a simple rigid band shift picture (hole doping, from Ru^{4+} to Ru^{5+}). One important ingredient, in the present case, might be the interaction among the different Ru(Ir)O₆-YO₆ octahedra. It is also possible that changes in the Coulomb interaction (Hubbard U) O $2p$–Ru $4d$ charge transfer energy (Δ) place SYR(I)O in a different region of the Zaanen-Sawatzky-Allen diagram [34]. Then, one important conclusion is the fact that the description of the electronic structure of SYR(I)O should be investigated, in a future work, taking into account many-body effects beyond the DFT method, but also treating explicitly the Ru(Ir)O₆-YO₆ interaction.

D. O 1*s* x-ray absorption spectra

The top panel of Fig. 5 shows the O $1s$ x-ray absorption spectra of Sr₂YRuO₆ and Sr₂YRu$_{0.75}$Ir$_{0.25}$O₆. The spectra are related to transitions from O $1s$ to empty O $2p$ states, which reflects the different metal bands, via hybridization. The structures at 529, 531, and 532 eV arise from O $2p$ states mixed with Ru $4d$ and/or Ir $5d$ states. In octahedral symmetry, the five Ru $4d$ (Ir $5d$) orbitals are split into the t_{2g} and e_g bands, as indicated in Fig. 5. From 533 to 540 eV, the O $2p$ states hybridize with Y $4d$ and Sr $4d$ states, and, at higher energies, the spectra are associated to an O $2p$–Ru $5sp$ combination. The main difference in the spectrum of each compound is the decrease in intensity of the first e_g peak, at 531 eV, relative to the second e_g peak, at 532 eV.

The bottom panel of Fig. 5 presents the calculated DOS projected on the unoccupied O $2p$ orbitals of Sr₂YRu$_{1-x}$Ir$_x$O₆. For $x = 0$, the partial DOS consists of a O $2p$ orbitals mixed with Ru $4d$ t_{2g}, at about 528.7 eV, and Ru $4d$ e_g, from around 530.7 to 532.4 eV. At higher energies, O $2p$ orbitals appear hybridized with Y $4d$ (533 eV), Sr $4d$ (535 eV), Y $4d$ (538 eV), and Ru $5sp$ (542 eV), as labeled in Fig. 5. For the $x = 0.25$ compound, the higher-energy region, above 533 eV, remains practically unchanged, whereas the lower-energy region has a new contribution from Ir $5d$ states. The Ir t_{2g} states show up
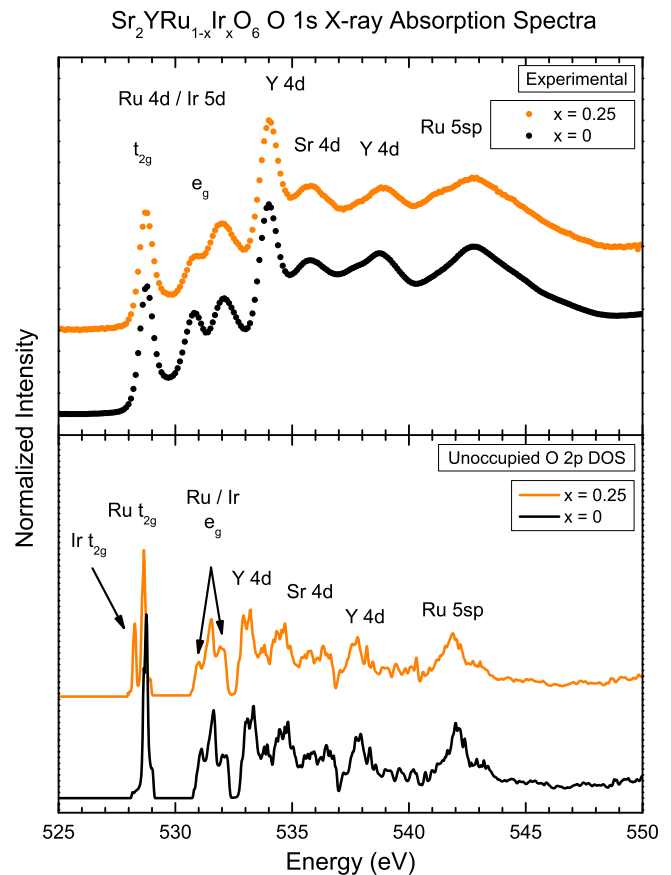

FIG. 5. O $1s$ x-ray absorption spectra of Sr₂YRuO₆ and Sr₂YRu$_{0.75}$Ir$_{0.25}$O₆. This technique is related to the O $2p$ unoccupied states, which are covalently mixed with different metal bands. The experimental spectra are compared to the calculated DOS projected into the unoccupied O $2p$ orbitals.

as a new peak in the DOS, at 528.2 eV, while the Ir e_g DOS contribute to the same region as the Ru e_g states.

The structures in the O $2p$ DOS are in good agreement with the O $1s$ XAS spectra. The discrepancies lie in the position of the higher-energy structures, which are are slightly underestimated, and in the central structure appearing in the e_g region. On the other hand, the decrease in the ratio of the first to second e_g peaks seen in the experimental data is reproduced by the DOS presented here. The two t_{2g} structures in the $x = 0.25$ DOS could not be resolved by the experiment, probably due to the experimental energy resolution.

E. Ground-state properties and density of states

The good agreement between the experimental and theoretical data shows that the calculation provides a satisfactory description of the electronic structure of SYR(I)O. Now, we proceed to the analysis of the ground-state properties and the total DOS. The ferromagnetic (FM) solutions resulted in total energies approximately 40 and 80 meV lower than the paramagnetic (P) solution for $x = 0$ and 0.25, respectively. In turn, the antiferromagnetic (AFM) solution yielded a total energy around 12 meV lower than the FM solution for the

TABLE I. Calculated and measured magnetic moments, in units of μ_B, for the Sr_2YRuO_6 compound.

	Calculated		NPD	
	This work	Ref. [22]	Ref. [7]	Ref. [5]
μ_{Tot}	0.00			
μ_{Ru}	1.66	1.70	1.96	1.85
$\mu_{O_{Ru}}$	0.10	0.10	0.06	

$x = 0$ compound, and about 20 meV lower for the $x = 0.25$ system.

The AFM solution for $x = 0$ resulted in magnetic moments of 1.66 μ_B/Ru ion and 0.10 μ_B/O ion. These results are in agreement the calculation presented in Ref. [22], as well as with data from neutron diffraction (NPD) experiments, as shown in Table I. On the other hand, the AFM solution for $x = 0.25$ actually resulted in a semiconducting and ferrimagnetic (FiM) ground state, with total magnetic moment of 1.99 μ_B/cell. For the RuO_6 octahedra, the calculated magnetic moments resulted in 1.65 μ_B/Ru, 0.10 μ_B/O$_{Ru}$, while for the IrO_6 octahedra the magnetic moments found are -0.45 μ_B/Ir and -0.04 μ_B/O$_{Ir}$.

To study the proposed canting of the magnetic moments in this system [6,12], the calculations shown here were performed for a magnetization axis **M** parallel to the b axis of the monoclinic structure, as suggested by neutron diffraction results [7]. In fact, these calculations indicate a total energy decrease of about 100 meV compared to calculations where **M** points along the pseudocubic b axis. These results suggest that the magnetic moments are indeed canted in the SYR(I)O system.

Figure 6 presents the calculated AFM densities of states of Sr_2YRuO_6 and $Sr_2YRu_{0.75}Ir_{0.25}O_6$. The majority and minority spin contributions to the DOS are displayed in the positive and negative y axis, respectively. The total DOS is projected into the Sr 4d, Y 4d, Ru 4d, Ir 5d, and O 2p orbitals, as indicated in the legend. In the top panel, the $x = 0$ DOS can be divided into four main regions. In the occupied states, the O 2p band extends from -6.2 to -1.2 eV, clearly presenting distinct bonding and nonbonding character. The antibonding Ru t_{2g} states appear from -1 eV to the Fermi energy largely mixed with O 2p states. On the positive energy region, the empty part of the Ru 4d t_{2g} states extends to 1 eV. A crystal-field splitting of roughly 10 Dq ~ 4.0 eV centers the Ru e_g states at around 3.5 eV, which are in turn split by J ~ 1 eV due to the intratomic exchange. The Y 4d and Sr 4d orbitals begin to contribute at around 5 eV.

The substitution of Ir for Ru causes changes in the DOS, as shown in the bottom panel of Fig. 6. At the bottom of the VB, the O 2p–Ir 5d bonding states appear between -6.7 and -5.2 eV, increasing the bandwidth of the O 2p band by approximately 0.4 eV. The occupied Ir 5d states with t_{2g} symmetry appear around the Fermi level, mixed with Ru 4d t_{2g} and O 2p states. The empty Ir 5d t_{2g} states are located just above the Fermi level, followed by the Ru 4d t_{2g} states from 0.1 to 1.1 eV. The unoccupied Ru 4d e_g band appears from 2.8 to 4.3 eV, mixed with Ir 5d e_g states from 3.3 to 4.3 eV. Further, Y 4d and Sr 4d states remain practically unchanged at higher
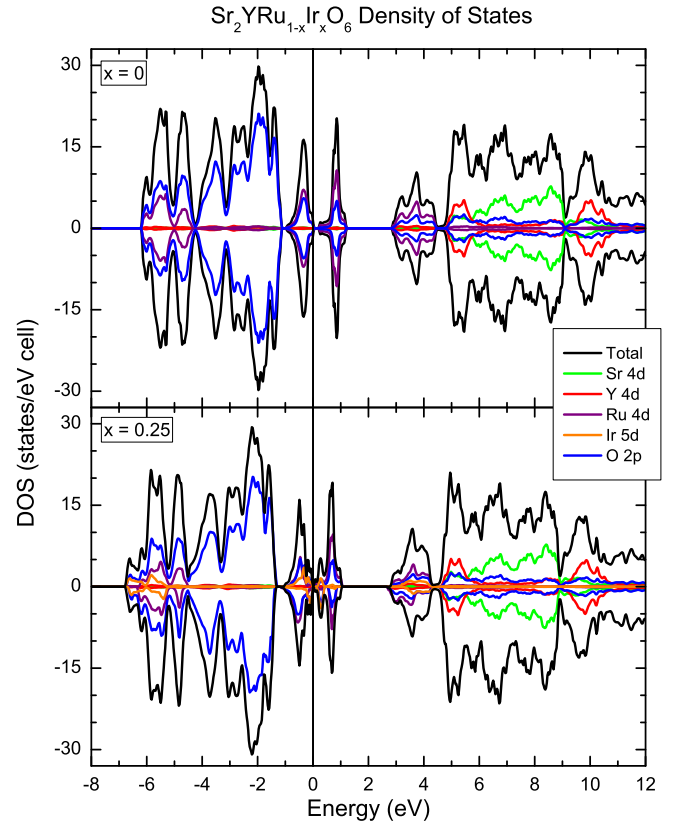

FIG. 6. Calculated densities of states (DOS) of Sr_2YRuO_6 and $Sr_2YRu_{0.75}Ir_{0.25}O_6$. The total DOS is projected into the Sr 4d, Y 4d, Ru 4d, Ir 5d, and O 2p orbitals, as well as in the majority and minority spin contributions.

energies. Finally, the calculated band gaps are around 0.24 and 0.10 eV for the pure and substituted compounds, respectively. The calculated gap for the $x = 0$ compound agrees with the measured value of around 0.1 eV [6].

F. Spin-orbit interaction

The growing interest in materials containing Ir lies in the new physics generated by the importance of spin-orbit (SO) coupling. The magnitude of the SO interaction ξ increases from 0.01 eV in 3d TMs to 0.1 eV in 4d TMs, and 0.5 eV in 5d TMs. Thus, this effect is negligible in 3d compounds, but it needs to be considered explicitly in 4d and 5d systems because it is of the same order as other interactions such as Coulomb and noncubic crystal fields [25,26,30].

Figure 7 compares the calculated DOS for $Sr_2YRu_{0.75}Ir_{0.25}O_6$ with and without the inclusion of spin-orbit coupling in the Ir 5d and Ru 4d valence orbitals. Each coupling was included separately, which is not shown here, but the real effect to the DOS comes only from the Ir 5d SO. As expected, the main change occurs from -1 to 1 eV region, which is dominated by Ru 4d and Ir 5d t_{2g} states. In the top panel of Fig. 7, the minority Ir 5d t_{2g} peak crosses the Fermi level, rendering this calculation a metallic ground state. The inclusion of the SO interaction, shown in the lower panel, is responsible for splitting this peak, suppressing the DOS at the Fermi energy to zero, which signals a tendency
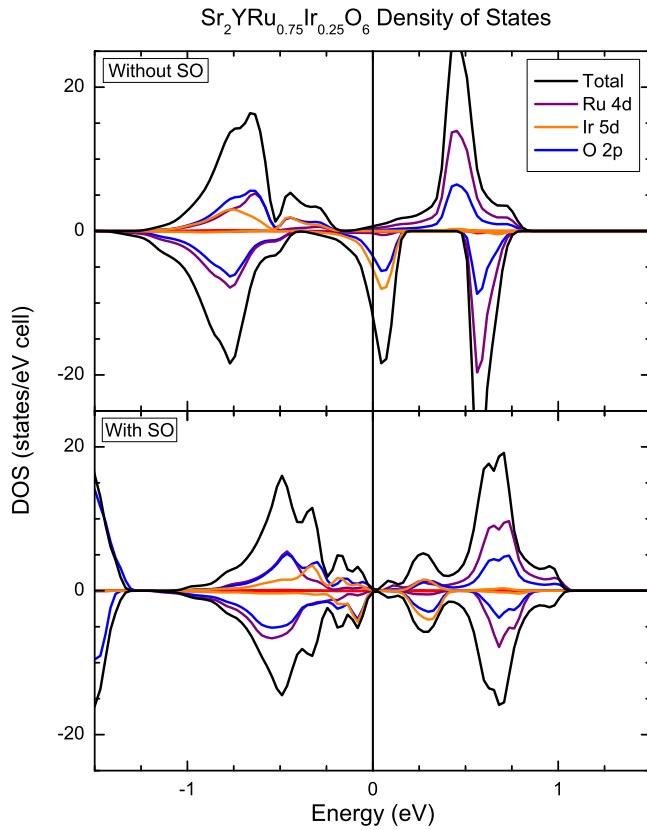
FIG. 7. Calculated densities of states for $Sr_2YRu_{0.75}Ir_{0.25}O_6$ with and without Ir $5d$ and Ru $4d$ spin-orbit coupling. The main effect comes from the inclusion of Ir $5d$ SO.

towards the true semiconducting behavior. This fact might be the signature of the enhancement of electron correlation due to SO coupling, as evident in the $Sr_{n+1}Ir_nO_{3n+1}$ series [27]. The two structures closer to the Fermi level are then assigned as the occupied and unoccupied parts of the so-called $j_{eff} = \frac{1}{2}$ state, as described in Ref. [29].

Another effect of the inclusion of the SO interaction is to reduce the magnetic moments within the IrO_6 octahedron, from 0.98 μ_B to 0.45 μ_B in Ir ions, and nearly suppressing all contribution of O ions. On the other hand, the effect on the magnetic moment within the RuO_6 octahedron is negligible, as shown in Table II. The importance of SO coupling in this material is also observed in inelastic neutron scattering [31].

The electron doping caused by the partial substitution of Ru $4d^3$ by Ir $5d^4$ raises the question of whether this extra electron delocalizes to other sites or, if it introduces any orbital

TABLE II. Calculated magnetic moments, in units of μ_B, of $Sr_2YRu_{0.75}Ir_{0.25}O_6$ and the effect of spin-orbit coupling.

	$x = 0.25$ (no SO)	$x = 0.25$ (SO)
μ_{Tot}	0.82	1.95
μ_{Ru}	1.63	1.65
$\mu_{O_{Ru}}$	0.10	0.10
μ_{Ir}	−0.98	−0.45
$\mu_{O_{Ir}}$	−0.10	−0.04

TABLE III. Calculated orbital occupancies of Sr_2YRuO_6 and $Sr_2YRu_{0.75}Ir_{0.25}O_6$, and the effect of spin-orbit coupling.

	$x = 0$	$x = 0.25$ (no SO)	$x = 0.25$ (SO)
Ru $4d$ t_{2g}	2.90	2.98	2.94
xy_{Ru}	0.97	1.01	0.97
xz_{Ru}	0.97	0.98	1.00
yz_{Ru}	0.96	0.99	0.97
Ir $5d$ t_{2g}		3.64	3.41
xy_{Ir}		1.25	1.17
xz_{Ir}		1.17	1.12
yz_{Ir}		1.22	1.12

anisotropy. This issue can be addressed by analyzing the orbital occupancy of the Ru $4d_{xy,xz,yz}$ and Ir $5d_{xy,xz,yz}$ orbitals, which are displayed in Table III. Neglecting the small deviation from the cubic perovskite structure, only these orbitals contribute to the t_{2g} molecular orbital. Since the energy convergence criterion was set to 10^{-6} eV, the digits displayed in Table III are exact up to the order of 10^{-4}.

According to the calculated data in Table III, the occupancy of the Ir t_{2g} orbital yielded 3.6 (3.4) electrons for the calculation without (with) SO coupling. Both values are smaller than the expected 4 electrons for the Ir^{5+} ion, implying a relatively strong hybridization effect in the Ir $5d$ states. Further, there is no evident sign of important orbital ordering, which indicates the system is quite isotropic. It is important to note that the occupation mentioned in Ref. [22] is related to the entire Ru $4d$ band, not only the t_{2g} symmetry as it was done here. Our analysis of the entire Ru $4d$ band (not shown) yielded similar results as in Ref. [22].

G. Discussion

It is known that in fcc magnetic lattices, such as the one formed by Ru^{5+} ions in Sr_2YRuO_6, next-nearest-neighbor (NNN) coupling and/or magnetic anisotropy can stabilize the magnetic order [8–10], although the latter should be much smaller than the former [9,10]. The existence of ferromagnetic interactions in SYRO was inferred from band-structure calculations [14] and proposed by several authors, albeit the microscopic origin of this interaction is still unclear. One hypothesis is that either single-ion magnetic anisotropy or antisymmetric superexchange interaction would cant spins and induce a small FM component [6,11,12]. On the other hand, the recently proposed picture of a partial long-range order, where alternate AFM layers are coupled, is indicative of sizable FM NNN interactions [7]. Although the described scenarios are fundamentally different, they are not mutually exclusive.

The discussion of magnetic interactions is not straightforward within the DFT framework. However, this method provides information on electron density and orbital occupancies, which can then be used to give insights on the magnetism of the system. The first-principles calculations reported here indicate a tilting of atomic spins away from the pseudocubic b' axis, and towards the monoclinic b axis, consistent with the spin canting picture. However, this canting induces no appreciable difference among the occupancies of Ru $4d$ t_{2g}, indicating a fairly isotropic character of the molecular bonds.

Also, according to the calculations, the magnetic moment of the Ir^{5+} ion is nearly 75% smaller than in Ru^{5+}. This fact is reflected in the induced magnetization of the oxygen ions at the IrO_6 octahedron, which are 60% smaller than the ones at the RuO_6 octahedron. Hence, the reduction of T_{N1} in the Ir substituted sample can be understood in terms of the weakening of the NNN interaction due to the decrease of the magnetic moment of Ir ion at 25% of the Ru sites. Further, the suppression of the fully ordered magnetic phase in the same compound can be understood in terms of the weakening of the Ru-O-O-Ru interaction due to the reduction of the spin polarization in oxygen sites, which reflects the characteristic strong Ru $4d$–O $2p$ covalency in this compound.

V. SUMMARY AND CONCLUSIONS

In this work, we report on physical properties, spectroscopy, and electronic structure of Sr_2YRuO_6 and $Sr_2YRu_{0.75}Ir_{0.25}O_6$ polycrystals. The spectroscopic methods used here were the x-ray (resonant) photoemission spectroscopy and x-ray absorption spectroscopy, which, to our knowledge, were never reported on these compounds. The experimental results were interpreted via first-principles calculations, with and without the inclusion of spin-orbit interactions.

In the valence band region, the x-ray photoemission spectra showed the O $2p$ and Ru $4d$ derived bands, which are clearly identified by the calculated density of states (DOS). The changes in the spectra caused by Ir substitution were also captured by the calculation, as evidenced by the increase

in the DOS close to E_F and at the bottom of the O $2p$ band. Furthermore, the contributions from Ru $4d$ orbitals to the valence spectra were identified with the Ru L_3 resonant photoemission technique. The difference between the on- and off-resonance spectra agreed well with the calculated Ru $4d$ DOS. The results showed that the Ru $4d$ (Ir $5d$) character appears close to the Fermi energy and is highly hybridized with O $2p$ states. Finally, the unoccupied part of the O $2p$ orbitals hybridized with different metal bands was mapped with the O $1s$ XAS.

The analysis of the calculated ground-state properties indicates that the spin-orbit interaction in Ir^{5+} ions causes a reduction of magnetic moments and renders $Sr_2YRu_{0.75}Ir_{0.25}O_6$ the correct semiconducting behavior, even though it does not induce any significant orbital ordering. Further, the presented reduction of T_{N1} with Ir substitution can be explained by the dilution of the magnetic moment in the $Sr_2YRu_{0.75}Ir_{0.25}O_6$ unit cell, specifically at the IrO_6 octahedra. Finally, the results show that the canting of Ru^{5+} magnetic moments could actually play an important role in the stabilization of the magnetic ordering in the Sr_2YRuO_6 system.

[1] J. M. Longo, J. Appl. Phys. **39**, 1327 (1968).

[2] Y. Maeno, H. Hashimoto, K. Yoshida, S. Nishizaki, T. Fujita, J. G. Bednorz, and F. Lichtenberg, Nature (London), **372**, 532 (1994).

[3] P. C. Donohue and E. L. McCann, Mater. Res. Bull. **12**, 519 (1977).

[4] R. Greatrex, N. N. Greenwood, M. Lal, and I. Fernandez, J. Solid State Chem. **30**, 137 (1979).

[5] P. D. Battle and W. J. Macklin, J. Solid State Chem. **52**, 138 (1984).

[6] G. Cao, Y. Xin, C. S. Alexander, and J. E. Crow, Phys. Rev. B **63**, 184432 (2001).

[7] E. Granado, J. W. Lynn, R. F. Jardim, and M. S. Torikachvili, Phys. Rev. Lett. **110**, 017202 (2013).

[8] Y.-Y. Li, Phys. Rev. **84**, 721 (1951).

[9] E. V. Kuzmin, S. G. Ovchinnikov, and D. J. Singh, Phys. Rev. B **68**, 024409 (2003).

[10] E. V. Kuz, S. G. Ovchinnikov, and D. J. Singh, J. Exp. Theor. Phys. **96**, 1124 (2003).

[11] R. P. Singh and C. V. Tomy, Phys. Rev. B **78**, 024432 (2008).

[12] P. L. Bernardo, L. Ghivelder, G. G. Eslava, H. S. Amorim, E. H. C. Sinnecker, I. Felner, J. J. Neumeier, and S. García, J. Phys.: Condens. Matter **24**, 486001 (2012).

[13] A. F. Garca-Flores, H. Terashita, E. M. Bittar, R. F. Jardim, and E. Granado, J. Raman Spectrosc. **45**, 193 (2014).

[14] I. I. Mazin and D. J. Singh, Phys. Rev. B **56**, 2556 (1997).

[15] H. A. Blackstead, J. D. Dow, D. R. Harshman, W. B. Yelon, M. X. Chen, M. K. Wu, D. Y. Chen, F. Z. Chien, and D. B. Pulling, Phys. Rev. B **63**, 214412 (2001).

[16] C. L. Chen, S. M. Rao, K. J. Wang, F. C. Hsu, Y. C. Lee, C. L. Dong, T. S. Chan, J. F. Lee, M. C. Ling, H. L. Liu, and M. K. Wu, New J. Phys. **11**, 073024 (2009).

[17] R. D. Shannon, Acta Crystallogr., Sect. A: Cryst. Phys., Diffr., Theor. Gen. Crystallogr. **32**, 751 (1976).

[18] B. H. Toby, J. Appl. Crystallogr. **34**, 210 (2001).

[19] A. C. Larson and R. B. von Dreele, General Structure Analysis System (GSAS), Los Alamos National Laboratory Report No. LAUR 86-748 (2004).

[20] M. Abbate, F. C. Vicentin, V. Compagnon-Cailhol, M. C. Rocha, and H. Tolentino, J. Synchrotron Radiat. **6**, 964 (1999).

[21] J. J. Yeh and I. Lindau, At. Data Nucl. Data Tables **32**, 1 (1985).

[22] G. K. H. Madsen, P. Blaha, K. Schwarz, E. Sjöstedt, and L. Nordström, Phys. Rev. B **64**, 195134 (2001).

[23] P. Blaha, K. Schwarz, G. Madsen, D. Kvasnicka, and J. Luitz, WIEN2K: An Augmented Plane Wave + Local Orbitals Program for Calculating Crystal Properties (2014), p. 1.

[24] J. P. Perdew, A. Ruzsinszky, G. I. Csonka, O. A. Vydrov, G. E. Scuseria, L. A. Constantin, X. Zhou, and K. Burke, Phys. Rev. Lett. **100**, 136406 (2008).

[25] B. J. Kim, H. Jin, S. J. Moon, J.-Y. Kim, B.-G. Park, C. S. Leem, J. Yu, T. W. Noh, C. Kim, S.-J. Oh, J.-H. Park, V. Durairaj, G. Cao, and E. Rotenberg, Phys. Rev. Lett. **101**, 076402 (2008).

[26] S. Y. Jang, H. Kim, S. J. Moon, W. S. Choi, B. C. Jeon, J. Yu, and T. W. Noh, J. Phys.: Condens. Matter **22**, 485602 (2010).

[27] S. J. Moon, H. Jin, K. W. Kim, W. S. Choi, Y. S. Lee, J. Yu, G. Cao, A. Sumi, H. Funakubo, C. Bernhard, and T. W. Noh, Phys. Rev. Lett. **101**, 226402 (2008).

[28] M. H. Aguirre, D. Logvinovich, L. Bocher, R. Robert, S. G. Ebbinghaus, and A. Weidenkaff, Acta Mater. **57**, 108 (2009).

[29] M. Wakeshima, D. Harada, and Y. Hinatsu, J. Alloys Compd. **287**, 130 (1999).

[30] G. Cao, T. F. Qi, L. Li, J. Terzic, S. J. Yuan, L. E. DeLong, G. Murthy, and R. K. Kaul, Phys. Rev. Lett. **112**, 056402 (2014).

[31] S. M. Disseler, J. W. Lynn, R. F. Jardim, M. S. Torikachvili, and E. Granado, Phys. Rev. B **93**, 140407 (2016).

[32] C. Guillot, Y. Ballu, J. Paigné, J. Lecante, K. P. Jain, P. Thiry, R. Pinchaux, Y. Pétroff, and L. M. Falicov, Phys. Rev. Lett. **39**, 1632 (1977).

[33] E. B. Guedes, M. Abbate, K. Ishigami, A. Fujimori, K. Yoshimatsu, H. Kumigashira, M. Oshima, F. C. Vicentin, P. T. Fonseca, and R. J. O. Mossanek, Phys. Rev. B **86**, 235127 (2012).

[34] J. Zaanen, G. A. Sawatzky, and J. W. Allen, Phys. Rev. Lett. **55**, 418 (1985).